

500 kV Gun Characterization Experiment: Phase I

D. Engwall, L. Cardman

June 4, 1996

1 Introduction

The Injector Test Stand (ITS) is designed to produce a 10 MeV, 135 pC/bunch, 5 mA average current electron beam suitable for injection into the proposed CEBAF free electron laser (FEL). It has been modelled [Li95] with the program PARMELA and is under construction. The beams produced by this injector in normal operation for the FEL will be substantially space charge dominated. Most of the transverse emittance growth experienced by these beams will occur during the first 50 cm of beamline, which consists of a 500 kV, GaAs photocathode electron gun, a single solenoidal lens, and a drift. Consequently, the ultimate quality of the ITS beam depends heavily upon the performance of the initial 500 keV beamline.

The final layout of the ITS includes minimal diagnostics for the 500 keV beamline. It is therefore essential that a gun characterization experiment be performed before the ITS is completed. An experiment measuring both the transverse and longitudinal phase space of the electron beam will have two immediate benefits. First, it will provide empirical data on the 500 keV beam, allowing enlightened planning for the optimization of the full ITS. Second, it will quantify PARMELA's ability to simulate intense, low energy beams accurately, thereby validating numerical simulations carried out with this code to optimize the complete FEL injector and providing confidence in future simulations of injector behavior in this regime of high bunch charge.

The first phase of this characterization experiment consists of measuring the transverse rms emittance ($\tilde{\epsilon}$) and rms momentum spread (δ) of the beams produced by the gun for a broad range of operating conditions. Before the ITS is completed, we will temporarily install a 500 keV diagnostics beamline a short distance downstream of the GaAs cathode. The measurements will be taken in a plane 155 cm downstream of the cathode for a variety of initial conditions (detailed below) and compared to PARMELA simulations duplicating the experimental conditions. In this technical note we begin by summarizing the layout of the experimental apparatus. Then we outline the parameter space available for our experiment, present the results of PARMELA simulations for this parameter space, and discuss their implications. Next we offer an estimate of the time required to complete the proposed set of measurements. Finally, we summarize the measurements and expected results.

2 Experimental Apparatus

The beamline for the characterization experiment is depicted in figure 1. It can be divided into two major sections: beam generation and beam diagnostics. The beam generation section has four major elements. The first element is the GaAs photocathode gun. It is followed immediately by a solenoidal lens to focus the emitted electron beam. This, in turn, is followed by an RF-shielded gate valve whose function is to provide vacuum isolation between the gun and the rest of the beamline when the gun is not operating or work is being done on the photocathode. The last component of the beam generation section is the light box. This device directs light from the Nd:YLF drive laser onto the GaAs wafer and deflects the light reflected from the wafer into a set of diagnostics for measuring laser power, position, etc.

The diagnostic beamline has been designed to measure $\tilde{\epsilon}$ and δ of space charge dominated beams via beam-intercepting techniques. A related experiment [Kepe] will measure the bunch length of these beams using a modified diagnostic beamline. In the transverse emittance measurement, a variant of the two-slit method is used. A water-cooled copper plug having a $100\ \mu\text{m}$ slit cut through it is scanned across the beam 155 cm downstream of the cathode. The 155 cm length allows us to focus the electron beam to a waist at or before the slit, and the $100\ \mu\text{m}$ slit-width ensures that the transmitted beamlet is emittance dominated. A wire scanner 55 cm downstream of the slit records the current distribution of each transmitted beamlet. With the spatial information gathered by the scanning slit and the angular distribution information gathered by the wire scanner, we can determine the emittance of the beam at the slit using the procedure outlined in [Le80]. In the momentum spread measurement, a small magnetic spectrometer is used. The same slit that is used in the emittance measurement serves as the object of a 45° spectrometer. The focal plane of the unit magnification spectrometer lies 57.88 cm downstream of the slit, and coincides with the location of another wire scanner. By measuring the rms beam width in the focal plane and folding in the dispersion of the spectrometer ($\sim 21\ \text{cm}$), we can infer the momentum spread of the beam at the slit.

The diagnostic beamline has four major elements. The first element is a six-way cross housing the slit mechanism and a beam viewer. It is followed by a 45° dipole magnet that is turned off for the transverse emittance measurement and turned on for the momentum spread measurement. Independent of which beamline leg is taken, the next two elements are identical: a five-way cross housing a wire scanner and a beam viewer, and an isolated Faraday cup used to measure beam current. This setup allows us to measure $\tilde{\epsilon}$ in a range from $\sim 0.1\ \pi\ \text{mm}\ \text{mr}$ to $\sim 10\ \pi\ \text{mm}\ \text{mr}$, and δ in a range from $\sim 0.1\%$ to $\sim 5\%$.

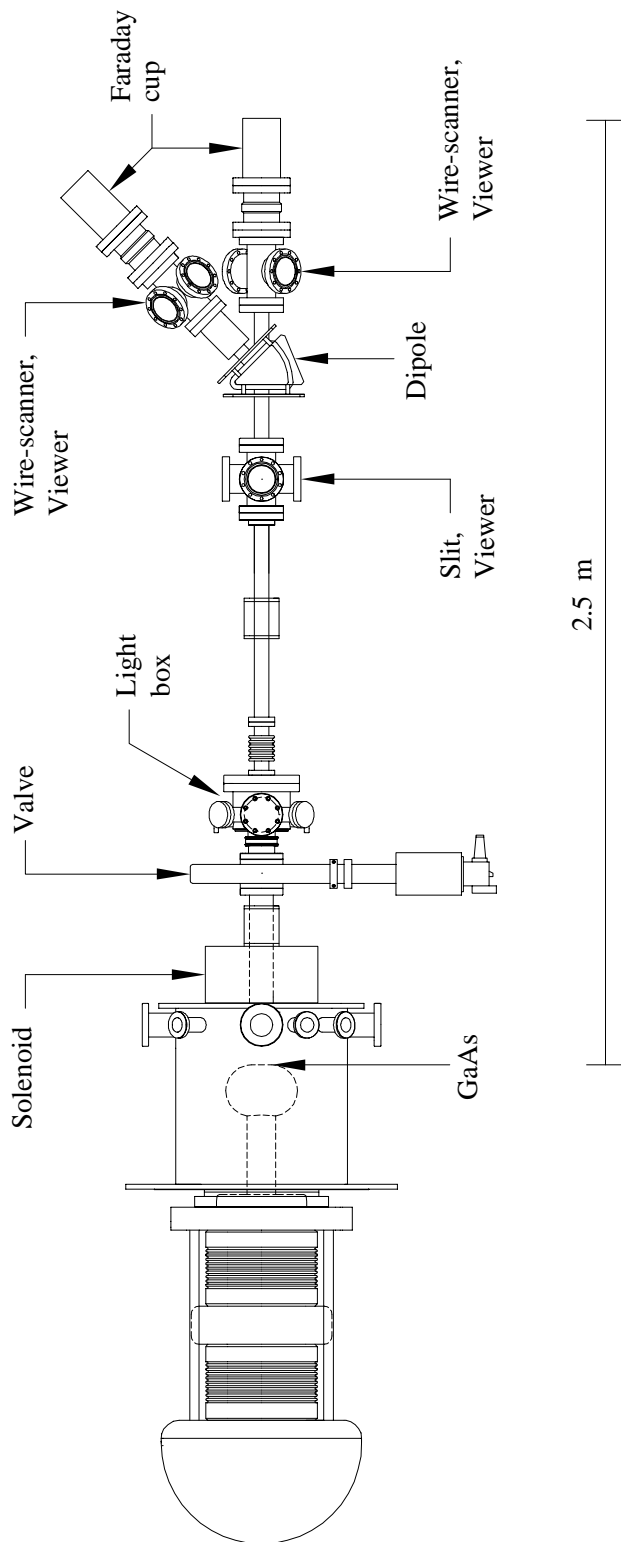


Figure 1: A plan view of the experimental apparatus for characterizing the beams generated by the 500 kV photocathode gun.

3 Available Parameter Space

The quality of the 500 keV beam (as characterized by $\hat{\varepsilon}$ and δ) depends upon the nature of the external fields seen by the beam, and on the beam's self-fields. The external fields present in the initial beamline consist of the electrostatic field in the anode-cathode gap and the magnetostatic field in the solenoid. While the field profile of the solenoid has been optimized (based on POISSON and PARMELA calculations) [Lipc] and is now fixed by mechanical constraints, the field profile in the gun can be altered through two operating variables: the distance separating anode and cathode, and the voltage between anode and cathode. The beam's self-fields are functions of the three operating variables that define the electron bunch: the initial radial charge distribution, the initial temporal charge distribution, and the total charge. These operating variables can be adjusted easily via the drive laser and its associated optics. We now describe the six parameters that allow us to control all operating variables.

The first two parameters pertain to details of the anode-cathode gap. They are the gap voltage, V_g , and the gap separation, d_g . The 550 kV Glassman Power Supply energizes the gap, providing voltages up to 500 kV with a stability of 10^{-4} . Thus V_g can take on any value from 0 V to 500 kV. The gun has been constructed with $d_g \approx 4.8$ cm, resulting in a maximum gradient of $E_{max} = 10$ MV/m on the GaAs wafer for $V_g = 500$ kV. The design of the gun allows the incorporation of a spacer nipple which increases the gap separation to $d_g \approx 10.6$ cm, resulting in $E_{max} = 6$ MV/m on the GaAs wafer for $V_g = 500$ kV. At the present time, these are the only two values d_g can assume.

The next two parameters concern the radial charge distribution of the beam at the cathode. They are the transverse cutoff of the beam, R_{max} , and the the transverse shaping factor of the beam, σ_r . Taken together, these two parameters affect the transverse size and uniformity of the initial electron beam. Figure 2 demonstrates this concept more clearly for two values of σ_r : R_{max} and $R_{max}/2$. The radial distribution of the initial laser pulse is a Gaussian of rms width σ_r . This initial Gaussian is passed through a circular aperture of radius R_{max} . The truncated Gaussian is then focussed on to the photocathode with unit magnification. The values that σ_r and R_{max} can assume are limited by the power dissipation capabilities of the aperture and the diffraction limits of the laser and the optical transport path. The range of values possible for σ_r and R_{max} varies from $\sim 1 \mu\text{m}$ up to ~ 5 mm.

The fifth parameter concerns the temporal charge distribution of the beam at the cathode. The temporal distribution of the incident laser pulse is a Gaussian of rms width σ_t , where σ_t is limited to a range of values between 15 ps and 25 ps by the capabilities of the modelocker in the drive laser. The true rms width of the beam's temporal distribution will be a convolution of the laser's σ_t and the GaAs wafer's rms response time, which has been measured to be less than 30–40 ps [We88, Al95]. Consequently, the rms length of the electron beam could exceed that of the incident laser pulse by a significant amount. During phase II of

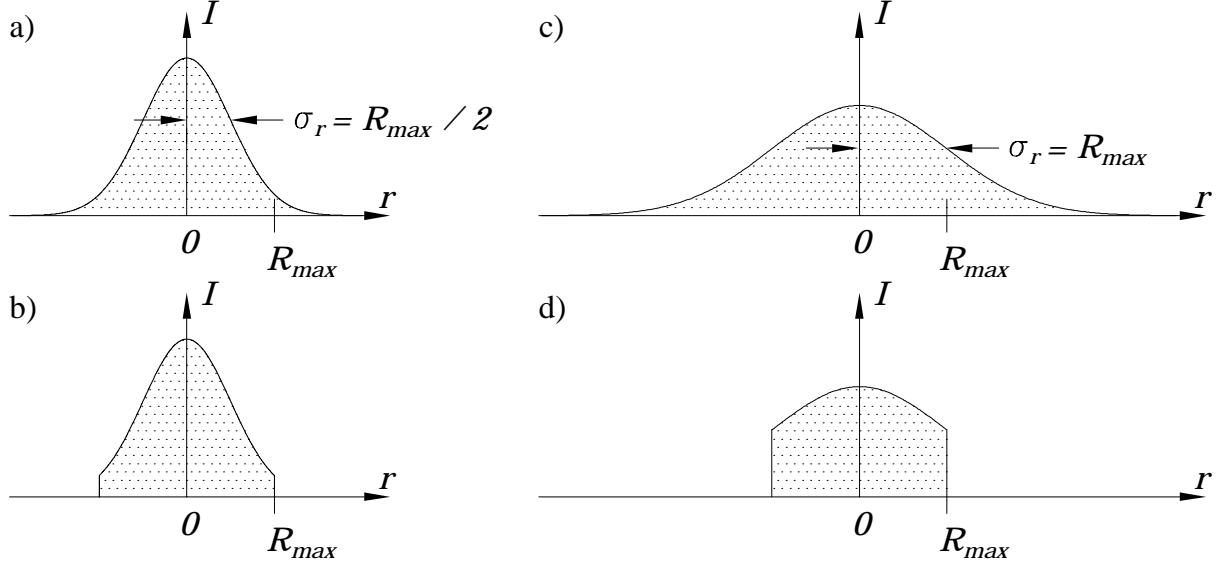


Figure 2: The radial distributions of Gaussian laser pulses of differing rms widths σ_r . Graphs a) and b) respectively show a pulse with $\sigma_r = R_{max}/2$ before and after an aperture of radius R_{max} . Graphs c) and d) show an equivalent-charge pulse with $\sigma_r = R_{max}$ before and after the same aperture, respectively.

the characterization experiment, the bunch length of the electron beam will be investigated carefully. If significant discrepancies occur between the rms length of the electron beam and laser pulse, we will repeat the PARMELA simulations using the measured temporal distribution. Until phase II has been completed, we will ignore the time response of the GaAs and estimate the rms width of the beam's initial temporal distribution by σ_t in our simulations.

The sixth parameter is the total charge in the pulse, q . The maximum total charge is limited by space charge forces at the cathode, by the ability to transport the bunch safely through the beamline, and by the drive laser power and the quantum efficiency (QE) of the photocathode. PARMELA simulations of the available parameter space (detailed below) can take into account the first two effects. These simulations indicate that the maximum amount of charge we should attempt to transport is ~ 1250 pC. When the drive laser is operated at its nominal power of 2 W we can expect to extract up to 200 pC/%QE from the photocathode. As a QE of 6% at 527 nm should be easily attainable, we anticipate no trouble in extracting bunches with charges up to ~ 1250 pC.

For our experiment, we will begin by varying the initial beam's transverse and temporal characteristics over the ranges of values outlined in Table 1 for a nominal excitation of $V_g = 500$ kV and $E_{max} = 10$ MV/m ($d_g \approx 4.8$ cm). For each of these 16 cases, we will vary the charge in the bunch from an emittance dominated regime (thus establishing a baseline $\tilde{\epsilon}$) to a space charge dominated regime, increasing the charge in a pulse until emittance growth limits our ability to transport the bunch through the system without scraping. Emittance

measurements will commence when sufficient charge is present within the beam to provide a baseline $\tilde{\epsilon}$ greater than $\sim 0.1 \pi$ mm mr, while momentum spread measurements will commence when sufficient charge is present to provide a δ greater than $\sim 0.1\%$. For the CEBAF FEL nominal case of $R_{max} = 1$ mm, $\sigma_r = R_{max}/2$, and $\sigma_t = 15$ ps, we will maintain the nominal gap separation of 4.8 cm and repeat the measurements for gap voltages of 400 kV and 300 kV ($E_{max} = 8$ MV/m and 6 MV/m, respectively). We will also repeat the measurements for this case with a gap voltage of 500 kV and a gap separation of 10.6 cm ($E_{max} = 6$ MV/m).

R_{max} (mm)	σ_r (mm)	σ_t (ps)
0.5	$R_{max}, R_{max}/2$	15, 25
1.0	$R_{max}, R_{max}/2$	15, 25
2.0	$R_{max}, R_{max}/2$	15, 25
4.0	$R_{max}, R_{max}/2$	15, 25

Table 1: Values of the radial and temporal parameterization of the beam that will be explored in the proposed experiment.

4 Simulations

We have used PARMELA to model the beam behavior for the sixteen cases listed in Table 1 for the 500 kV, 10 MV/m setup. We have also modelled the beam behavior for the CEBAF FEL nominal case ($R_{max} = 1$ mm, $\sigma_r = R_{max}/2$, and $\sigma_t = 15$ ps) for the V_g and d_g setups described above. We performed the modelling according to the procedures outlined in Appendix A. In this section we present the results of these simulations in graphical form. Note that the simulations presented in figures 3–6 and 8–10 do not include the effects of image charge in the plane of the cathode or in the beam pipe, while those presented in figures 7 and 11 do. The simulations depicted by figures 7 and 11 were performed after the other simulations when it had been discovered that the image-charge effects had a noticeable (factor of ~ 3) impact on the maximum amount of charge that could be extracted from the photocathode. As demonstrated in appendix B, the inclusion of image charge has only a $\sim 5\%$ effect on the determination of δ , and a $\sim 10\%$ effect on the determination of $\tilde{\epsilon}$. Given the level of uncertainty already present in the simulations due to the unknown response time of the GaAs photocathode, we feel confident that the results of the simulations performed without image-charge effects are sufficiently accurate for the scope of this technical note, whose primary purpose is to delineate the magnitude of the effects we expect to observe and to define the measurement plan.

In figures 3 and 4, we plot $\tilde{\epsilon}$ as a function of the initial pulse peak current for $\sigma_r = R_{max}$

and $\sigma_r = R_{max}/2$, respectively. The expected behavior of the curves is observed. As the peak current is increased by three orders of magnitude, the emittance grows by two orders of magnitude. At low peak currents, space charge effects are negligible and the emittance varies with the transverse extent of the spot on the cathode. As beam current increases and space charge effects assert themselves, the emittance values increase. Because the space charge effects are more acute in smaller diameter beams, we see enhancement in the rate of emittance increase with bunch charge first for the 0.5 mm, then for the 1 mm, then for the 2 mm, and finally for the 4 mm diameter beams. Note that the space charge effects at large peak currents reverses the ordering of the emittance values.

In figure 5, we plot the ratio of $\tilde{\epsilon}_{R_{max}}$ to $\tilde{\epsilon}_{4mm}$ against initial peak current to show the effects of initial beam diameter. The graph contains curves for $R_{max} = 0.5$ mm, 1 mm, and 2 mm in the case where $\sigma_r = R_{max}$ and $\sigma_t = 15$ ps. The shape of the curves can be explained as follows. In the low peak current regime, the beams are emittance dominated and the ratio should equal $R_{max} / 4$ mm. In our graph the ratios closely approximate the ideal values; discrepancies are due to the limited number of macroparticles simulated ($\sim 10^3$). As the current in the bunches increases, space charge forces exert themselves and the emittance increases. Because the space charge effects are more marked in the smaller-diameter beams, they experience emittance growth first and the ratio increases. However, as the current rises further, the space charge forces tend to increase the beam's diameter; thereby lessening the space charge forces and facilitating solenoidal compensation [Ca89] at the measurement plane of the emittance growth that occurs in the anode-cathode gap. The enhanced space charge in the smaller-diameter beams causes them to expand faster, permitting a higher degree of solenoidal compensation so that the rate of increase in the ratio of emittances will slow or even go negative. Furthermore, as the diameter of the (initially) smaller-diameter bunches increases more rapidly than that of the 4 mm radius beam, the (initially) smaller-diameter bunches are affected by solenoidal aberrations before the (initially) larger-diameter bunches. Therefore the ratio can again increase sharply (as is observed for the 1 mm and 0.5 mm cases at peak currents of ~ 5 and 3 A, respectively).

In figure 6a, we plot the ratio of $\tilde{\epsilon}_{25ps}$ to $\tilde{\epsilon}_{15ps}$ as a function of initial peak current to show the effects of temporal duration. The shape of the curves can be interpreted in the following way. The ratios in the low-charge, emittance dominated regime are unity. While both the $\sigma_t = 15$ ps and $\sigma_t = 25$ ps pulses have the same peak current, the longer pulses contain more charge in their tails. The larger amount of tail-charge causes a higher degree of variation in the self forces along the length of the pulse, resulting in a higher rate of emittance growth in the longer pulses as bunch charge is increased. Consequently, as the current is increased and space charge forces become appreciable, the ratio increases monotonically. Because the space charge effects are more acute in smaller diameter beams, we see the ratio increase first for the 0.5 mm, then the 1 mm, then the 2 mm, and finally the 4 mm diameter beams.

In figure 6b, we plot the ratio of $\tilde{\epsilon}_{\sigma_r=R_{max}/2}$ to $\tilde{\epsilon}_{\sigma_r=R_{max}}$ vs initial peak current for bunches with identical initial R_{max} to show the effects of transverse uniformity. The shape of the

curves can be explained as follows. Initially the ratios for the emittance dominated regime should be clustered at 0.86 due to the intrinsically higher emittance of the $\sigma_r = R_{max}$ bunches. The discrepancies seen in our calculations are again due to the limited number of superparticles simulated ($\sim 10^3$). As more charge is placed in the bunches, the $\sigma_r = R_{max}/2$ bunches have a more nonlinear space charge force than the $\sigma_r = R_{max}$ bunches (see appendix C). Therefore the ratio initially increases. However, as even more charge is included in the bunches, space charge forces and anodic defocussing conspire to increase the beam's diameter and divergence. Upon entering the solenoid, the $\sigma_r = R_{max}/2$ bunches have a smaller diameter than the $\sigma_r = R_{max}$ bunches (mostly due to their lower intrinsic emittance), and a correspondingly lower divergence (due to a reduced level of anodic defocussing derived from their smaller diameter). The smaller diameter of the $\sigma_r = R_{max}/2$ bunches is offset by their lower divergence, thereby allowing them to attain a higher degree of solenoidal compensation than the $\sigma_r = R_{max}$ bunches. Consequently, the ratio levels out or even decreases. As even more charge is included in the bunches, the smaller divergence of the $\sigma_r = R_{max}/2$ bunches can no longer offset their smaller diameter at the solenoid entrance and the $\sigma_r = R_{max}$ bunches attain the higher degree of solenoidal compensation. At this point, the ratio again increases.

In figure 7a, we plot $\tilde{\epsilon}_n$ as a function of initial pulse peak current in the case $R_{max} = 1$ mm, $\sigma_r = R_{max}/2$, and $\sigma_t = 15$ ps for a variety of anode-cathode conditions. Four V_g (E_{max}) conditions are considered: 500 kV (10 MV/m), 400 kV (8 MV/m), 300 kV (6 MV/m), and 500 kV (6 MV/m). The expected behavior of the curves is observed. As the peak current is increased by two orders of magnitude, the normalized rms emittance grows by a factor of 50.

In figure 7b, we plot the ratio of $\tilde{\epsilon}_{n,V_g(E_{max})}$ to $\tilde{\epsilon}_{n,500(10)}$, the normalized rms emittance for the anode-cathode condition 500 kV (10 MV/m). The ratios are plotted against initial peak current for the anode-cathode conditions of 500 kV (6 MV/m), 400 kV (8 MV/m), and 300 kV (6 MV/m) to show the effects of the field in the anode-cathode gap. The shapes of the curves are interesting. Initially, all ratios have a value of unity (within the accuracy of the calculations), as they should in the low-current, emittance dominated regime. As the current in the bunches increases, the space charge forces cause the emittance to increase. Due to their reduced rigidity, the lower energy/peak-field bunches are more heavily influenced by the space charge forces so the ratio initially increases; the lower energy bunches are affected because they are everywhere less rigid than the 500 kV (10 MV/m) bunches, while the lower peak-field pulses are affected because they are less rigid than the 500 kV (10 MV/m) bunches in the anode-cathode gap. The ratio turns up first for the 300 kV, then the 400 kV, and finally for the 500 kV (6 MV/m) case as expected. As the current rises further, the space charge forces increase the beam diameter; thereby lessening space charge forces and allowing solenoidal compensation of the emittance growth. As space charge effects are felt more acutely in less rigid beams, the 300 kV, 400 kV, and 500 kV (6 MV/m) beams expand faster than the 500 kV (10 MV/m) beam so that they experience a higher degree of compensation; consequently the ratio decreases. For even higher currents, the 500 kV (10 MV/m) beam expands enough to undergo as large a degree of compensation as the less rigid beams, so the

ratio flattens out or increases slightly. In the 400 kV case, solenoidal aberrations cause the ratio to increase sharply at currents of ~ 5 A. Finally, we note that solenoidal compensation allows the 500 kV (6 MV/m) case to outperform the 500 kV (10 MV/m) case by $\sim 10\%$ in the regime of current required for the CEBAF FEL.

In figures 8 and 9, we plot δ against initial pulse peak current for $\sigma_r = R_{max}$ and $\sigma_r = R_{max}/2$, respectively. The expected behavior of the curves is observed. As the peak current is increased by two orders of magnitude, the momentum spread grows by a factor of 50. The tightness of the curves indicates that while the transverse and longitudinal phase spaces are probably coupled, they have insufficient time to mix appreciably in our very short beamline.

In figure 10a, we plot the ratio of δ_{15ps} to δ_{25ps} as a function of pulse charge to show the effects of temporal duration. The shape of the curves can be explained as follows. As the peak current in the bunches is increased, the longitudinal tails of the longer bunch contain more charge than the tails of the shorter bunch. As a consequence, the longitudinal space charge forces are stronger in the longer bunch than the shorter bunch. Therefore the momentum spread of the longer bunch grows faster and the ratio increases.

In figure 10b, we plot the ratio of $\delta_{\sigma_r=R_{max}/2}$ to $\delta_{\sigma_r=R_{max}}$ as a function of initial peak current to show the effects of transverse uniformity. As expected, there is little ($\sim 5\%$) variation in δ due to the small amount of mixing between the coupled transverse and longitudinal phase spaces.

In figure 11, we plot δ against initial pulse peak current in the case $R_{max} = 1$ mm, $\sigma_r = R_{max}/2$, and $\sigma_t = 15$ ps for a variety of anode-cathode conditions. Four V_g (E_{max}) conditions are considered: 500 kV (10 MV/m), 400 kV (8 MV/m), 300 kV (6 MV/m), and 500 kV (6 MV/m). The expected behavior of the curves is observed. Due simply to their enhanced rigidity, the 500 kV cases exhibit smaller momentum spreads than the 400 kV case, which in turn has a smaller momentum spread than the 300 kV case. Furthermore, the 500 kV (10 MV/m) case shows a slightly better momentum spread than the 500 kV (6 MV/m) case due to the latter's larger d_g (which increases both the length of the beamline and the amount of time the electrons spend at energies less than 500 keV).

5 Time Estimates

Because of time constraints on the realization of the full ITS, it is useful to estimate the amount of time required to complete the proposed measurements. If we assume that the gun functions flawlessly throughout the experiment, the time required to do the experiment is dominated by the amount of time the wire scanner spends scanning.

We now calculate the time requirements of a worst-case wire scanner scan. Typically, emit-

tance and momentum spread measurements necessitate the scanning of about 15 beamlets passed by the slit mechanism. In a worst-case scenario, the wire scanner must step through 1 cm wide beamlets with a resolution of $60\ \mu\text{m}$; the wire scanner must take 167 steps. Bowling has estimated [Bopc] that the EPICS calls necessary for each step will require about 1 sec. Additionally, after each step, the current must be read from the wire. This should require about 2 sec to allow the wire motion to damp and the gated integrator–boxcar averager to acquire a statistically meaningful number of pulses. Consequently, one wire scanner pass will need 501 sec.

The time required for the entire experiment can now be calculated in a straightforward manner. We will investigate 19 cases, where each case involves measuring $\tilde{\epsilon}$ and δ no more than ~ 10 times. The total time is therefore

$$\begin{aligned} 19 \text{ cases} \times 10 \frac{\text{runs}}{\text{case}} \times 15 \frac{\text{passes}}{\text{run}} \times 501 \frac{\text{sec}}{\text{pass}} &= 1.43 \times 10^6 \text{ sec} \\ &= 397 \text{ hr} . \end{aligned}$$

We therefore conclude that phase I of the gun characterization experiment (if carried out at the same level of detail as presented in this note) will take about 50, eight-hour-working-days.

6 Summary

We will measure $\tilde{\epsilon}$ and δ as functions of R_{max} , σ_t , and σ_r as outlined in Table 1. We will also make these measurements as functions of q , V_g , and d_g . For both measurements there are some limitations on the amount of charge that can be transported through the system. For all cases where $R_{max} = 0.5\ \text{mm}$, the range of peak currents in the experiment extends from a low of $\sim 10\ \text{mA}$ to a high of $\sim 7\ \text{A}$. Similarly, for all cases where $R_{max} = 1\ \text{mm}$, the range of peak currents in the experiment extends from a low of $\sim 10\ \text{mA}$ to a high of $\sim 13\ \text{A}$. And for all cases where $R_{max} = 2\ \text{mm}$ or $4\ \text{mm}$, the range of peak currents in the experiment extends from a low of $\sim 10\ \text{mA}$ to a high of $\sim 20\ \text{A}$. Note that these current values pertain to cathode fields of $E_{max} = 10\ \text{MV/m}$; they must be derated accordingly for smaller E_{max} . PARMELA predicts dramatic growth in the beam emittance and momentum spread as we vary the current from very low values through the normal operating values for the FEL (typically a factor of ~ 50 for both $\tilde{\epsilon}$ and δ). The code further predicts that as we change the aspect ratio and the uniformity of our beams in the manner outlined in Table 1 (while maintaining a constant peak current in the initial beam) we can expect to see effects of order 10–50% in the emittance measurements and the momentum spread measurements involving longitudinal changes, but smaller effects (~ 5 –20%) in the momentum spread measurements involving transverse changes. Finally, PARMELA anticipates effects up to order $\sim 30\%$ in the emittance measurements and up to order $\sim 50\%$ in the momentum spread measurements as we change the anode-cathode parameters V_g and d_g .

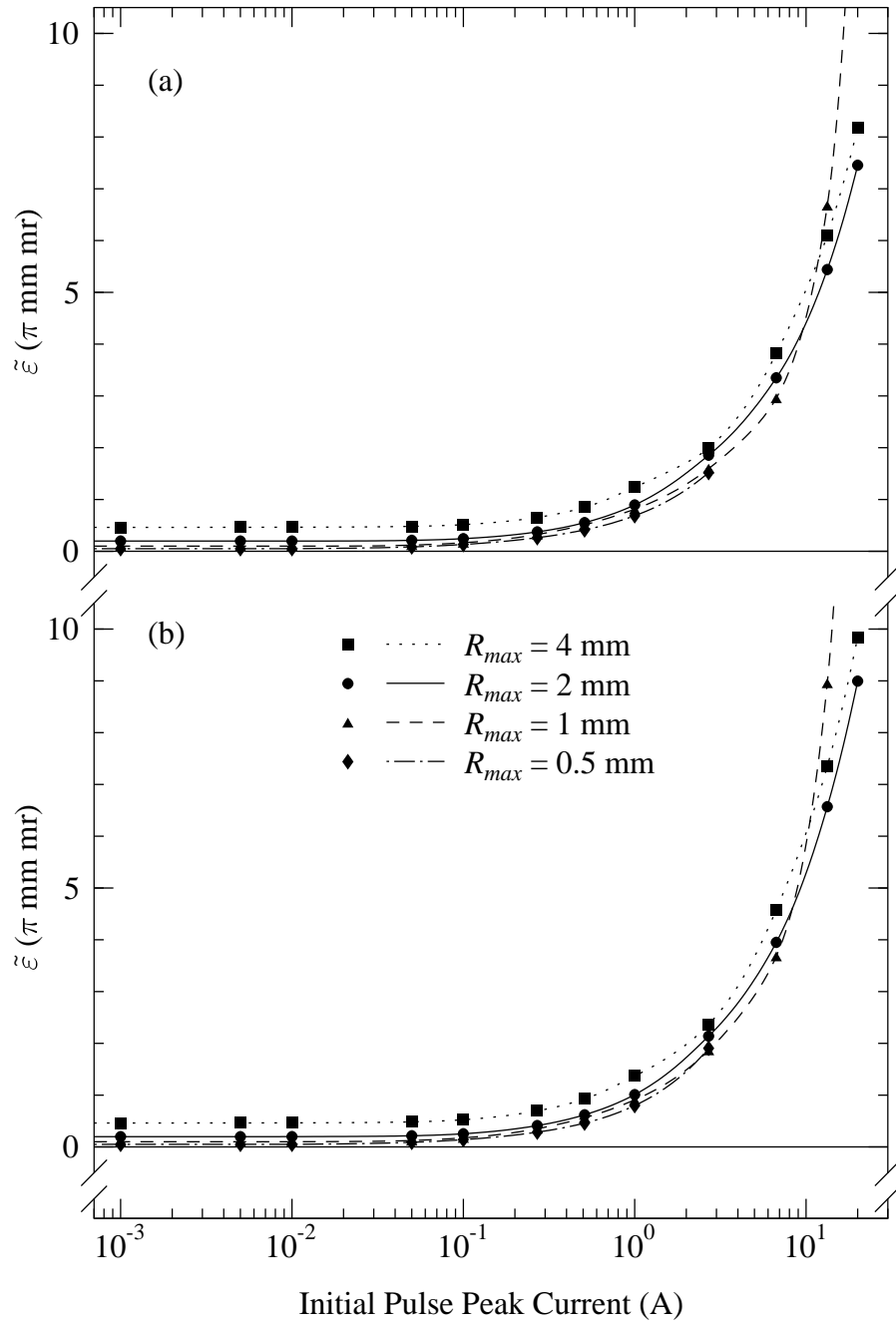


Figure 3: Transverse rms emittance as a function of initial pulse peak current for $\sigma_r = R_{max}$. Graph (a) shows the results for $\sigma_t = 15$ ps and graph (b) shows the results for $\sigma_t = 25$ ps.

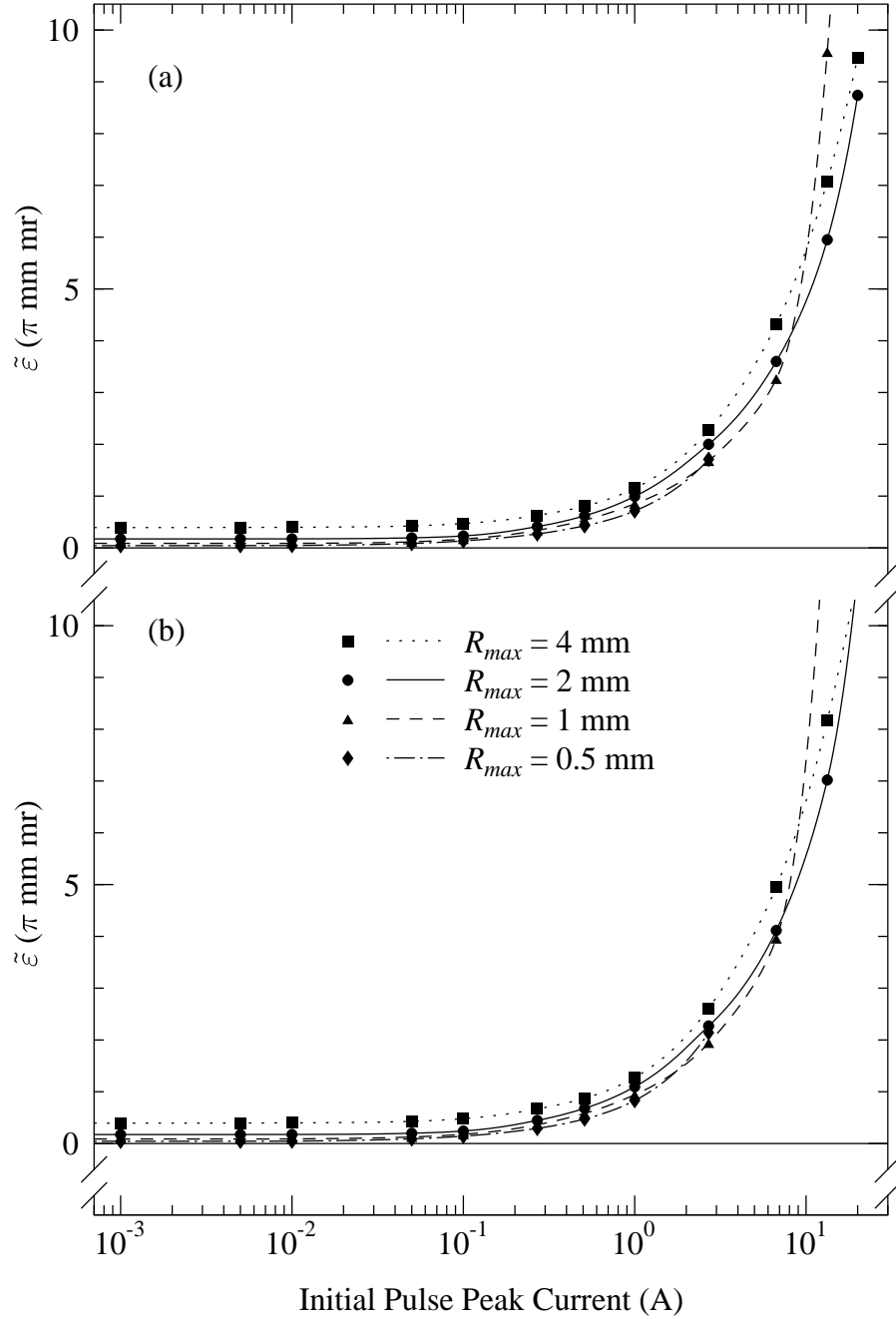


Figure 4: Transverse rms emittance as a function of initial pulse peak current for $\sigma_r = 2R_{max}$. Graph (a) shows the results for $\sigma_t = 15 \text{ ps}$ and graph (b) shows the results for $\sigma_t = 25 \text{ ps}$. Note that the nominal values for the CEBAF FEL ($R_{max} = 1 \text{ mm}$, $\sigma_r = R_{max}/2$, and $\sigma_t = 15 \text{ ps}$) are indicated by the triangles in graph (a).

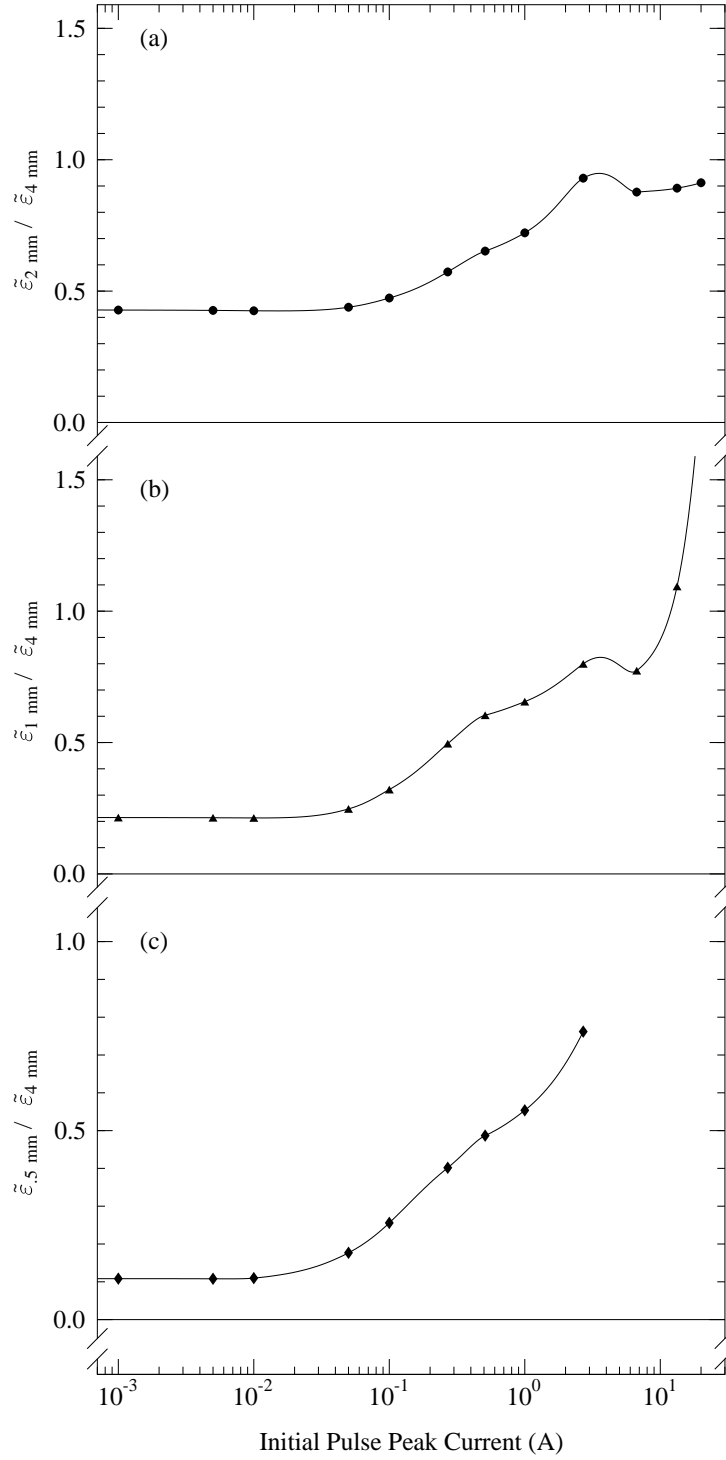


Figure 5: Expected variations in the rms emittance for the case $\sigma_r = R_{max}$ and $\sigma_t = 15 \text{ ps}$. The graph shows the effects of initial spot size by comparing a) $R_{max} = 2 \text{ mm}$, b) $R_{max} = 1 \text{ mm}$, and c) $R_{max} = 0.5 \text{ mm}$ to $R_{max} = 4 \text{ mm}$ pulses.

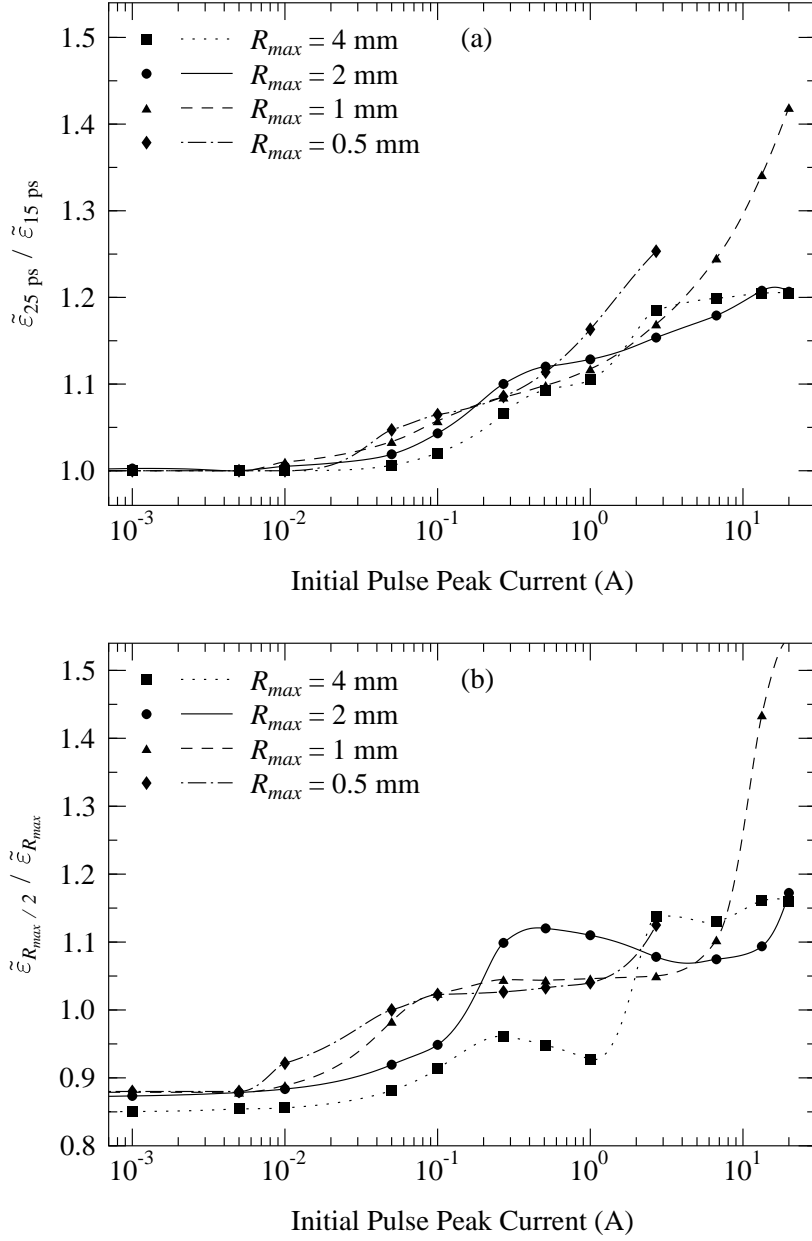


Figure 6: Expected variations in the rms emittance. Graph (a) shows the effects of temporal duration by comparing $\sigma_t = 15 \text{ ps}$ and $\sigma_t = 25 \text{ ps}$ pulses for $\sigma_r = R_{max}$. Graph (b) shows the effects of transverse uniformity by comparing $\sigma_r = R_{max}$ and $\sigma_r = R_{max}/2$ pulses for $\sigma_t = 15 \text{ ps}$.

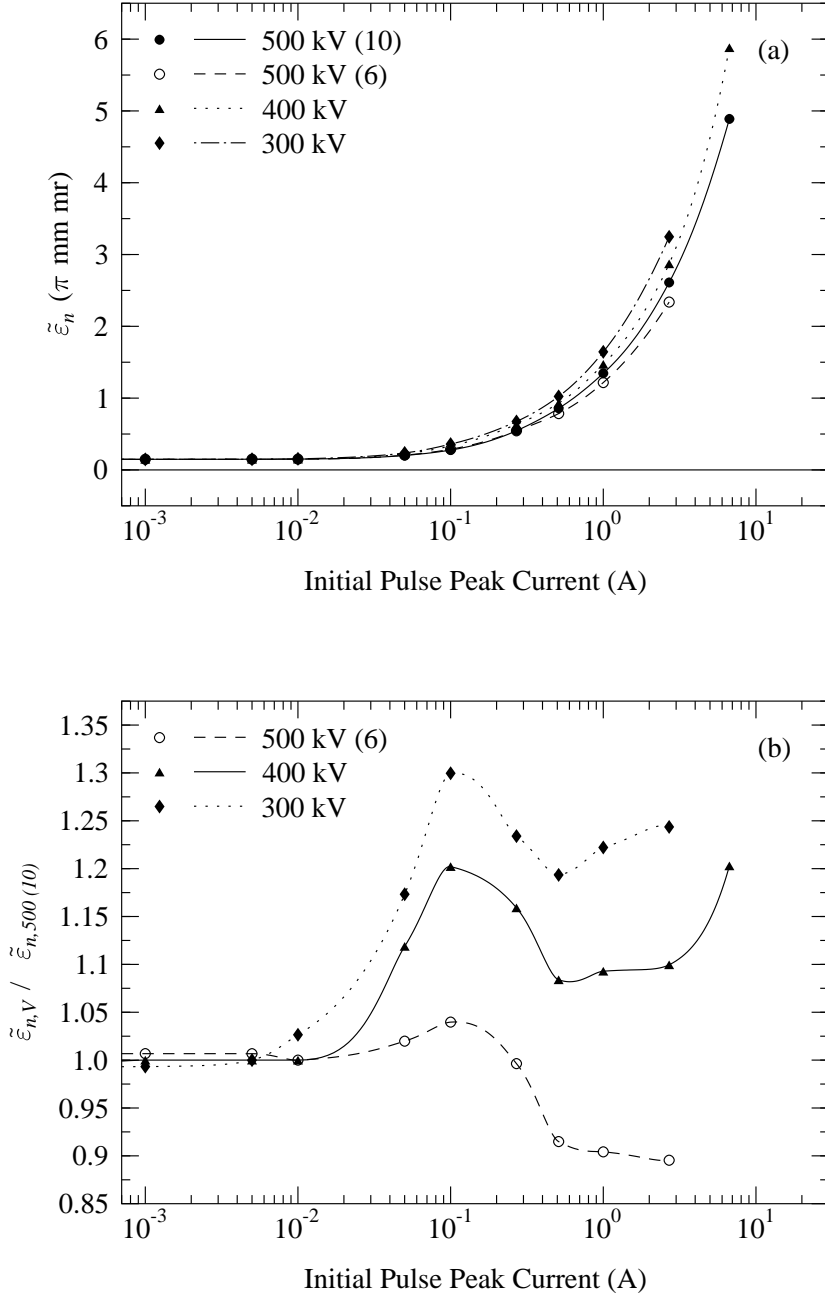


Figure 7: Expected variations in the normalized rms emittance for the case $R_{max} = 1$ mm, $\sigma_r = R_{max}/2$, and $\sigma_t = 15$ ps under a variety of anode-cathode conditions. Graph (a) shows the normalized rms emittance as a function of initial peak current. Graph (b) shows the expected variations in the normalized rms emittance by comparing pulses of different V_g or E_{max} to nominal 500 kV, 10 MV/m pulses.

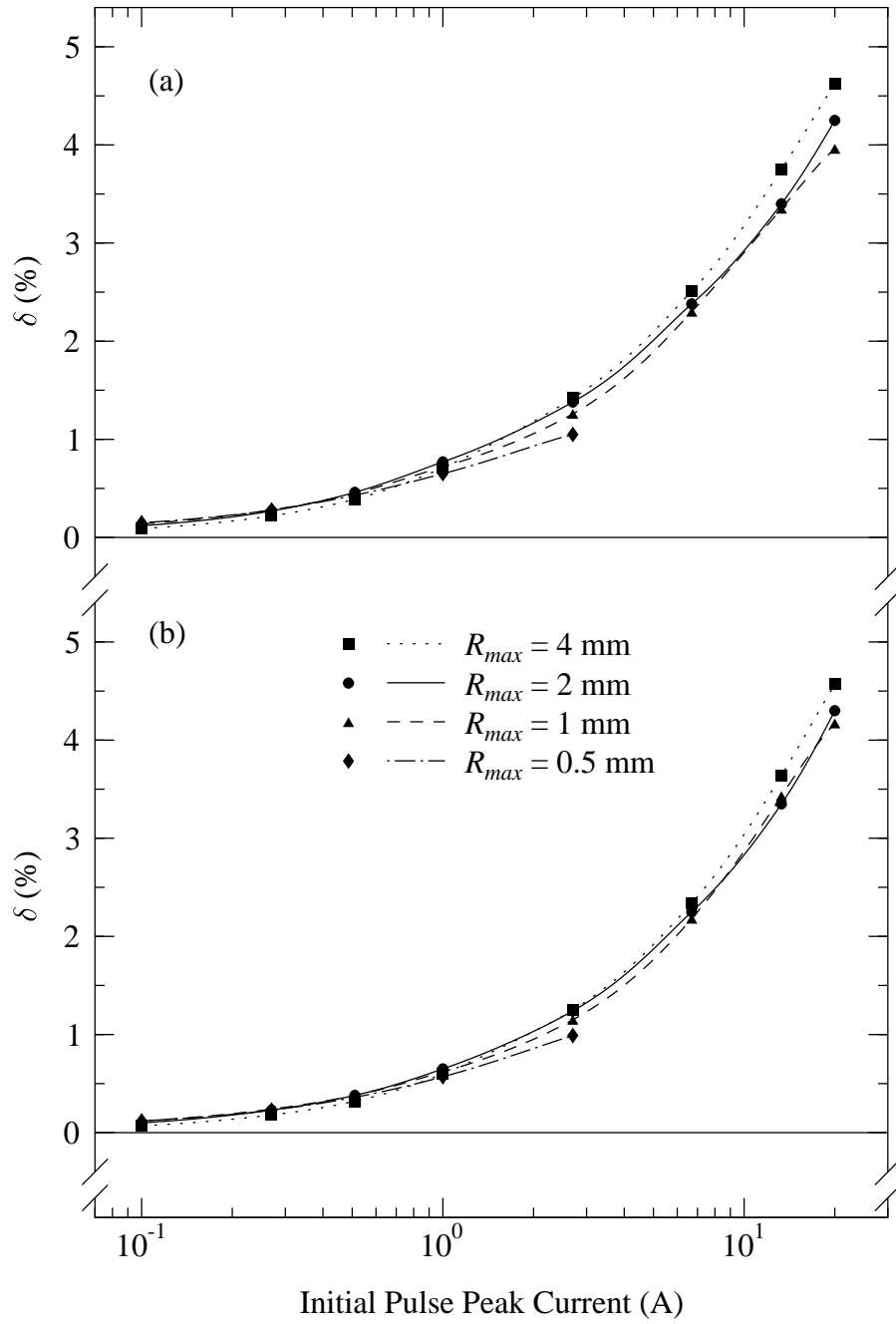


Figure 8: RMS momentum spread as a function of initial pulse peak current for $\sigma_r = R_{max}$. Graph (a) shows the results for $\sigma_t = 15$ ps and graph (b) shows the results for $\sigma_t = 25$ ps.

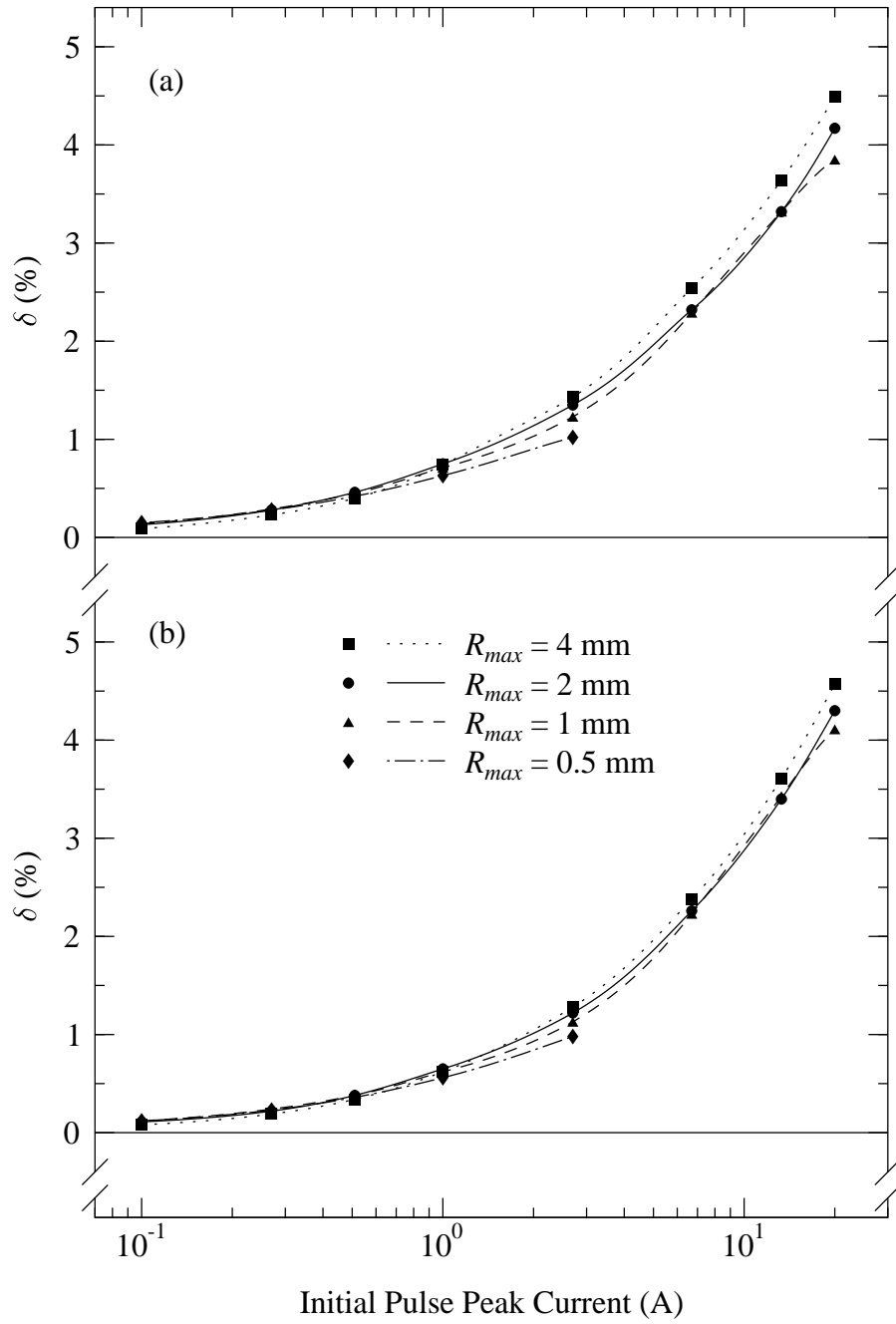


Figure 9: RMS momentum spread as a function of initial pulse peak current for $\sigma_r = R_{max}/2$. Graph (a) shows the results for $\sigma_t = 15$ ps and graph (b) shows the results for $\sigma_t = 25$ ps.

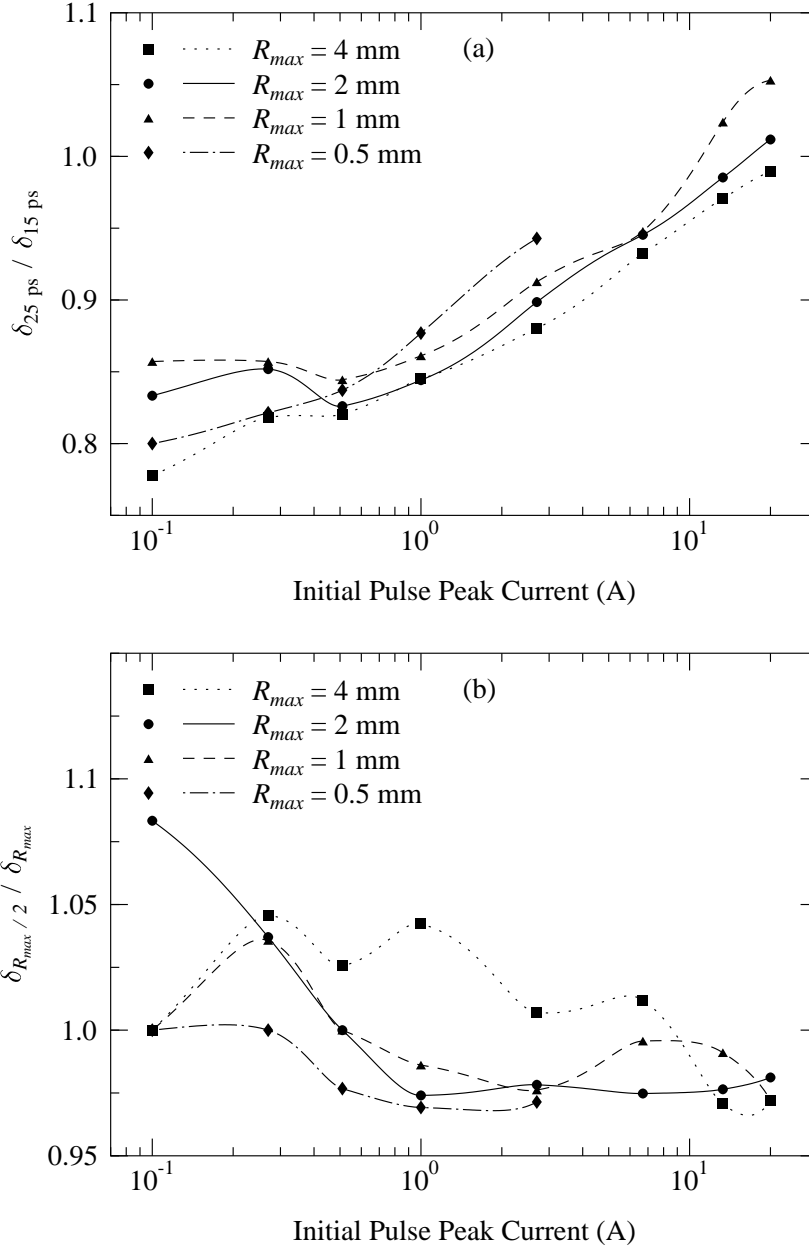


Figure 10: Expected variations in the rms momentum spread. Graph (a) shows the effects of temporal duration by comparing $\sigma_t = 15 \text{ ps}$ and $\sigma_t = 25 \text{ ps}$ pulses for $\sigma_r = R_{max}$. Graph (b) shows the effects of transverse uniformity by comparing $\sigma_r = R_{max}$ and $\sigma_r = R_{max}/2$ pulses for $\sigma_t = 15 \text{ ps}$.

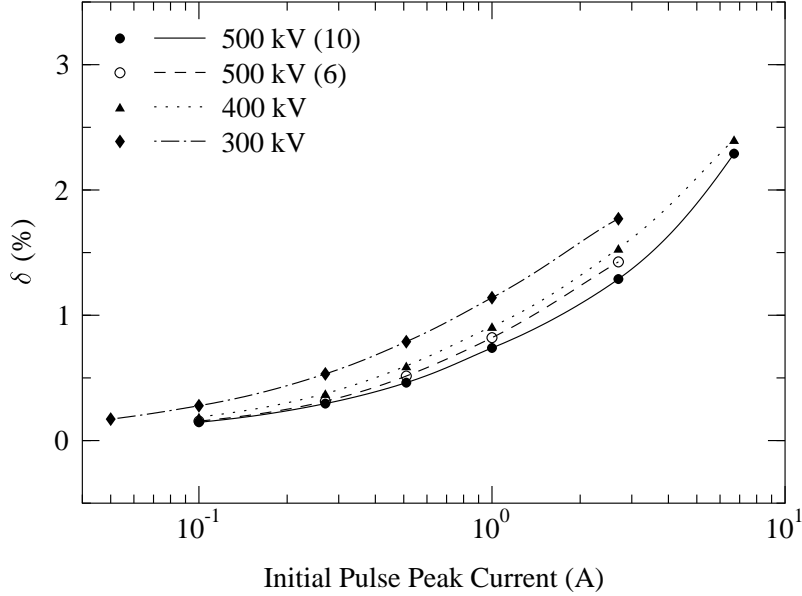


Figure 11: RMS momentum spread as a function of initial peak current for the case $R_{max} = 1$ mm, $\sigma_r = R_{max}/2$, and $\sigma_t = 15$ ps under a variety of anode-cathode conditions.

A Appendix: PARMELA Modelling

In this appendix we present the layout and procedures used in modelling our beam with PARMELA for the 16 cases under study.

A.1 The Layout

The PARMELA input file defining the runs can be broken into four logical units: gun, drift 1, solenoid, and drift 2. In the ensuing discussion, we use the following dimensional format. A dimension occurring by itself is common to both the $E_{max} = 10$ MV/m and the $E_{max} = 6$ MV/m setups, while a dimension followed by another dimension enclosed in parentheses refers to a dimension in the 10 MV/m setup (a dimension in the 6 MV/m setup).

1. Gun: This element, of length 9.48944 cm (15.24 cm), extends from $z = 0$ cm to $z = 9.48944$ cm ($z = 15.24$ cm). It contains the POISSON calculated electrostatic field profile E_r, E_z for the anode/cathode structure of the 500 kV gun. The E_r, E_z field pairs were calculated on a square r, z grid of side 0.2032 mm for a cathode potential of -500 kV.

2. Drift 1: This element, of length 0.01388 cm (0.01642 cm), extends from $z = 9.48944$ cm to $z = 9.50332$ cm ($z = 15.24$ cm to $z = 15.25642$ cm). Its purpose is to serve as a book-keeping buffer between the end of the gun's field profile and the beginning of the solenoid's field profile.
3. Solenoid: This element, of length 37.38 cm, extends from $z = 9.50332$ cm to $z = 46.88332$ cm ($z = 15.25642$ cm to $z = 52.63642$ cm). It contains the POISSON calculated magnetic field profile B_r, B_z for the solenoid designed [Lipc] to be used in this experiment. The B_r, B_z field pairs were calculated on a square r, z grid of side 0.6 mm. It is of interest to note that the physical center of this solenoid is located at $z = 23.90332$ cm (this permits the upstream edge of the solenoid casing to coincide with the exterior edge of the gun chamber's downstream flange). This means that this solenoid's downstream field profile is 8.58 cm longer than its upstream profile. It was discovered [Lipc] that unless the integration step size in the solenoid were sufficiently small, a small, net angular velocity is imparted to the beam upon its passing through the solenoid. In order to keep the time required to do the simulations reasonable, we decided to include the extra 8.58 cm of field profile on the downstream side to counteract the induced angular velocity, instead of changing the integration step size. The solution chosen solved the problem and had a negligible effect on the optics of the runs (due to the fact that the added length is so far out into the fringe field).
4. Drift 2: This element, of length 111.11668 cm, extends from $z = 43.88332$ cm to $z = 155$ cm ($z = 52.63642$ cm to $z = 163.7531$ cm). The end of this element corresponds to the location of the copper slit that is used in the emittance and momentum spread measurements. This element is chosen to be sufficiently long to allow the beam to be brought to a waist within this drift so that the beam is diverging at the slit.

A.2 The Procedure

For each of the 16 cases under study, 1000 superparticles are tracked from the cathode to the measurement plane (copper slit). The dynamics calculations utilize the variable-size point-by-point space charge algorithm [Li94] with a maximum particle size factor of 10. Currently, only a portion of the simulations include the effects due to image charges in the plane and beam pipe. The steps involved in each simulation are identical:

1. Launch the 1000 macroparticles making up the electron beam from the cathode at $z = 0$ into the gun. The cathode emission routine in PARMELA launches the charge-weighted macroparticles with Gaussian profiles in both the radial and longitudinal directions and with a Maxwellian energy distribution. For all cases, the kinetic energy distribution is identical: a Gaussian centered on 0.1 eV with an rms width of 0.03 eV. The rms width of the transverse (longitudinal) direction is σ_r (σ_t), while the radius

(half-length) at which the distribution is cut off is $R_{max}(3\sigma_t)$. The total charge carried by the bunch is q .

2. Integrate the macroparticles through the gun, drift 1, the solenoid, and drift 2. The integration step size in the gun and the solenoid is 1° of the 1497 MHz fundamental frequency, while the step size in the drift regions is 4° . Note that the strength of the solenoid is varied to achieve a diverging beam at the slit.
3. Using the particle coordinates at the end of drift 2, calculate the exact $\tilde{\epsilon}$ and δ of the beam there.

B Appendix: Image Charge Effects

In this appendix we demonstrate the effects of including image charge in our calculations. We have performed two sets of simulations for the CEBAF FEL nominal case ($R_{max} = 1$ mm, $\sigma_r = R_{max}/2$, and $\sigma_t = 15$ ps): one set including the image charge effects, and one set ignoring the image charge effects. We present the results of these simulations in figure 12.

There are four plots in figure 12. In graphs (a) and (b) we plot $\tilde{\epsilon}$ and δ respectively, as a function of initial pulse peak current for both sets of simulations. In graph (c) we plot the ratio of $\tilde{\epsilon}$ from the set including image effects to $\tilde{\epsilon}$ from the set ignoring image effects against initial peak current. In graph (d) we plot the ratio of δ from the set including image effects to δ from the set ignoring image effects against initial peak current.

Several inferences can be drawn from the data presented in figure 12. First, we see that the inclusion of image charge decreases the maximum amount of extractable charge in a pulse by up to a factor of ~ 3 . Its effect on $\tilde{\epsilon}$ and δ is much smaller. Neglecting image charge effects can cause an overestimation of $\tilde{\epsilon}$ by up to $\sim 12\%$ and an underestimation of δ by no more than $\sim 5\%$. We therefore conclude that the effect of image charge in our modelling has a negligible impact on the determination of $\tilde{\epsilon}$ and δ , and a large effect on the determination of the maximum amount of extractable charge in a pulse. We note that the trends of $\tilde{\epsilon}$ and δ vs peak current plotted in figures 3–6 and 8–10 for various initial conditions should be correct, but most of these curves can be expected to be cutoff at maximum peak currents roughly a factor of three smaller than shown. We further note that all future simulations will include image charge effects in an attempt to improve the accuracy of maximum-charge estimation.

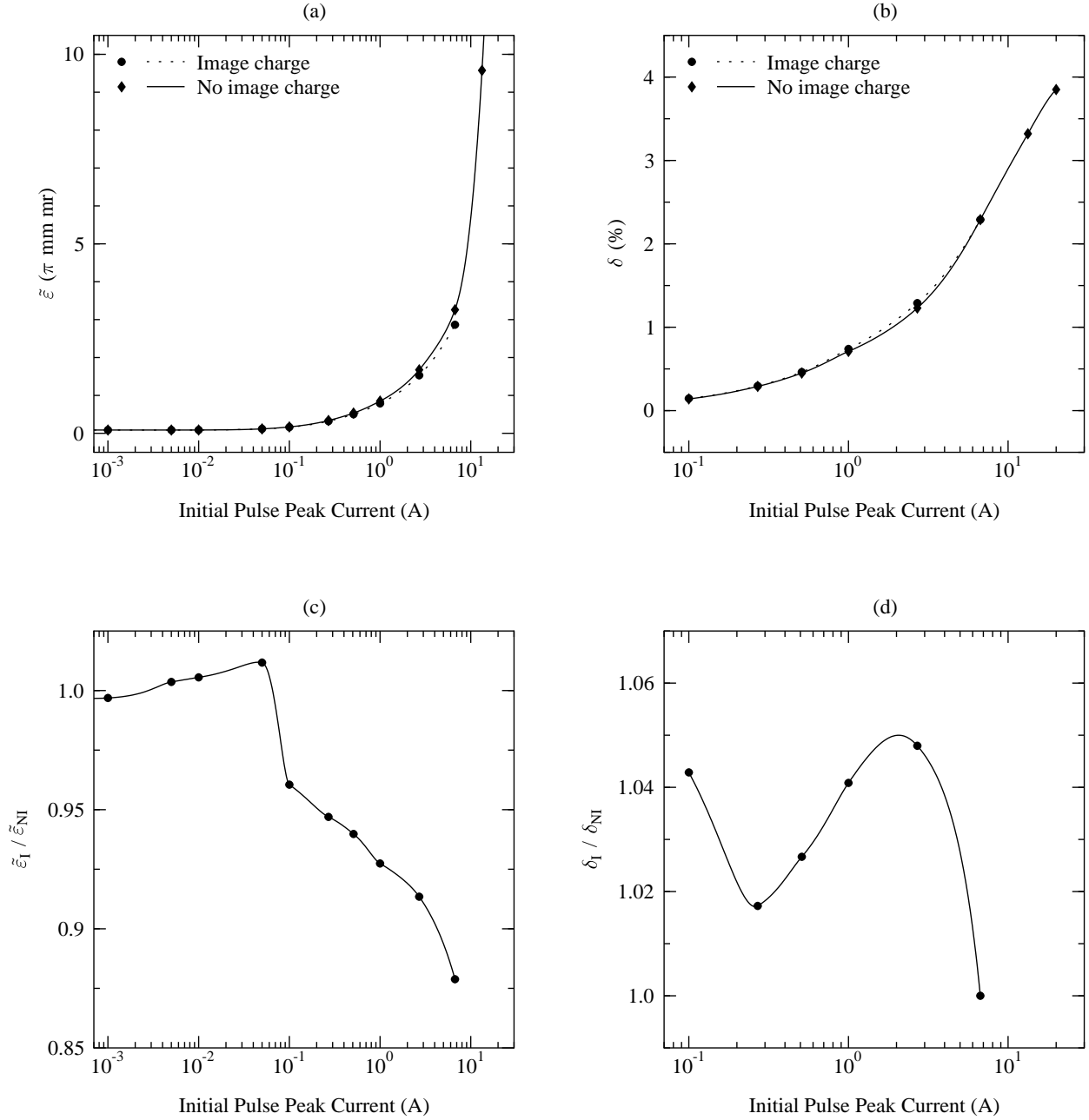


Figure 12: Expected variations in the transverse rms emittance and rms momentum spread under differing image charge contributions. Graph (a) shows the rms emittance as a function of initial peak current. Graph (b) shows the rms momentum spread as a function of initial peak current. Graph (c) shows a direct comparison of rms emittances calculated in the presence of image charges ($\tilde{\epsilon}_I$) and in the absence of image charges ($\tilde{\epsilon}_{NI}$). Graph (d) shows a direct comparison of rms momentum spreads calculated in the presence of image charges (δ_I) and in the absence of image charges (δ_{NI}).

C Appendix: Space Charge Fields

In figure 13 we plot the radial space charge force within an infinitely long beam as a function of radial displacement (r/R_{max}) from the optic axis. The three cases shown correspond to a uniform transverse charge density, a Gaussian transverse charge density truncated at $1\sigma_r$ ($\sigma_r = R_{max}$), and a Gaussian transverse charge density truncated at $2\sigma_r$ ($\sigma_r = R_{max}/2$). All three beams have the same radius and contain equal amounts of charge. Clearly the space charge force of the $\sigma_r = R_{max}$ beam is more linear than that of the $\sigma_r = R_{max}/2$ beam.

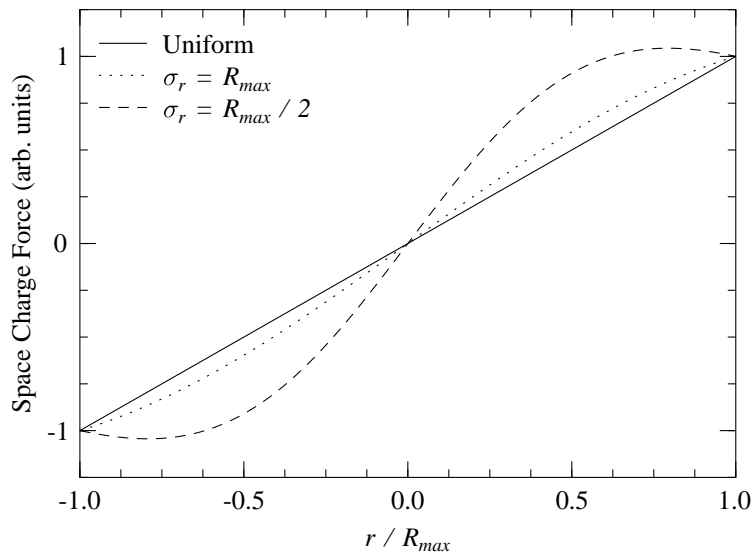


Figure 13: Radial space charge force within an infinitely long beam as a function of radial displacement from the optic axis. The graph shows curves for three different transverse charge distributions: uniform, $\sigma_r = R_{max}$ Gaussian, and $\sigma_r = R_{max}/2$ Gaussian.

References

- [Al95] A.V. Aleksandrov, *et al*, Phys. Rev. E, **51** (2), 1449–1452 (1995).
- [Bopc] B. Bowling, personal communication.
- [Ca89] B.E. Carlsten, Nucl. Instr. and Meth., **A285**, 313–319 (1989).
- [Kepc] D. Kehne, personal communication.

- [Le80] C. LeJeune and J. Aubert, “Emittance and Brightness: Definitions and Measurements,” in *Applied Charged Particle Optics*, A. Septier, Ed., Advances in Electronics and Electron Physics, Supp. **13A**, 159–259 (1980).
- [Li94] H. Liu, CEBAF–TN–94–040, July (1994).
- [Li95] H. Liu, *et al*, *Proc. 1995 Part. Accel. Conf.*, in publication.
- [Lipc] H. Liu, personal communication.
- [We88] J.J. Welch, SLAC-PUB-4517, January (1988).